Applied Catalysis B: Environmental 337 (2023) 122999

Contents lists available at ScienceDirect

Applied Catalysis B: Environmental

journal homepage: www.elsevier.com/locate/apcatb

Synthesis of nitriles by the electro-oxidative coupling of primary alcohols and ammonia on Pd nanoparticle-modified CuO nanowires in oxidant-free electrolytes under ambient conditions

Zhiyong Fang [a], Yunxuan Ding [b], Mei Wang [a], Linqin Wang [b], Fusheng Li [a], Ke Fan [a], Xiujuan Wu [a], Licheng Sun [a,b], Peili Zhang [a,*]

[a] State Key Laboratory of Fine Chemicals, Institute of Artificial Photosynthesis, DUT-KTH Joint Education and Research Centre on Molecular Devices, Dalian University of Technology, Dalian 116024, China

[b] Center of Artificial Photosynthesis for Solar Fuels and Department of Chemistry, School of Science, Westlake University, Hangzhou 310024, China

ARTICLE INFO

Keywords:
Coupling reactions
Electrooxidation
Nitriles
Electrosynthesis
Nanocatalysts

ABSTRACT

Developing green strategies for the synthesis of nitriles from cheap starting materials, without toxic and hazardous reagents under mild conditions is important for the sustainable development of the chemical industry. Herein, we report an oxidant- and cyanide-free catalytic system for the synthesis of various nitriles via electro-oxidative coupling of corresponding primary alcohol and ammonia in an aqueous solution with Pd nanoparticle-modified CuO nanowires as the catalyst. Produce benzonitrile from benzyl alcohol achieve a conversion of > 99.0 % and a selectivity of 83.2 %. Mechanism studies demonstrate that the coupling of surface-adsorbed active species NH_2 * and Ph-CHO* is the rate-limiting step, and the Pd/CuO heterojunction is the active center. The electrogenerated Cu^{III} species provide the driving force for oxidation, and Pd contributes to improving the dehydrogen ability and facilitating the subsequent coupling reaction. Our research provides an environment-friendly oxidative C-N coupling method for efficient nitriles electrosynthesis.

1. Introduction

Nitriles are important intermediates in the synthesis of numerous products, such as herbicides, agrochemicals, pharmaceuticals, and polyester material [1–4]. Moreover, the nitrile group serves as a versatile precursor for various functional groups, such as amines, amidines, tetrazoles, aldehydes, amides, and other carboxylic derivatives [5,6]. Several strategies have been developed for nitrile production, including the Sandmeyer reaction (Scheme 1a) [7,8], Rosenmund-von Braun reaction (Scheme 1b), [9,10] nucleophilic substitution of alkyl and aryl halides (Scheme 1c) [11–15], oxidation of amines (Scheme 1d) [16,17], and dehydration of amides and aldoximes (Scheme 1e) [18,19]. Generally, these methods require toxic or hazardous reagents and harsh reaction conditions, and also generate chemical wastes. Therefore, an environment-friendly route for the synthesis of nitriles from cheap starting materials under mild conditions is strongly demanded.

In the absence of cyanide, the C≡N functional group is usually formed through the transformation of a -CH_2-OH- or -CHO group by coupling with a nitrogen source. These conversion reactions involve hydrogen and/or oxygen elimination, C-N coupling, and the formation of unsaturated bonds, which are thermodynamically difficult and involve high energy consumption. Therefore, these transformations require stoichiometric amounts of sacrificial oxidants, and high reaction temperatures to drive the reactions. New developments in this field are focused on the direct synthesis of nitriles through the catalytic aerobic ammoxidation reaction of alcohols and ammonia in the presence of oxygen (Scheme 1f) [20–30]. However, the use of oxygen needs sealing and high-pressure equipment, which increases the cost and danger of the reaction. Therefore, an oxidant-free synthesis system for nitriles is desired, to overcome the existing drawbacks of the catalytic ammoxidation reaction.

Herein, we demonstrate an effective electrochemical strategy for the direct synthesis of nitriles from alcohols and ammonia in an aqueous solution under ambient conditions without the use of oxidants (Scheme 1g). In this system, Pd nanoparticle-modified CuO nanowires (Pd@CuO) were used as the catalyst. Under optimal conditions, nitriles were efficiently synthesized with a conversion efficiency of 75–99 %, and a selectivity of 55–84 % based on alcohol. In situ analysis and theoretical

* Corresponding author.
E-mail address: peilizhang@dlut.edu.cn (P. Zhang).

https://doi.org/10.1016/j.apcatb.2023.122999
Received 11 January 2023; Received in revised form 12 June 2023; Accepted 13 June 2023
Available online 15 June 2023

calculations show that the highly-efficient catalytic performance originates from the synergy between the Pd nanoparticles and CuO nanowires. The Pd@CuO heterojunction provides a unique stage for the cascade oxidation reaction between alcohols and ammonia and finally induces the formation of nitriles. Under the applied conditions, CuO is electrooxidized to Cu^{III}, which drives the oxidation and proton elimination steps. Pd plays an important role in stabilizing the Cu^{III} species and in tailoring the selective adsorption capacity of alcohols and ammonia.

2. Experimental methods

2.1. Solvents and reagents

The chemicals and solvents were purchased from commercially available sources and used without further purification.

2.2. Synthesis of palladium nanoparticles supported on CuO nanowires (Pd@CuO nanowires)

The synthesis of Pd@CuO nanowires refers to previous literature [31] and the experimental process was improved on this basis. The copper sulfate pentahydrate ($CuSO_4$•5 H_2O) and ammonium hydroxide (NH_3·H_2O) were dissolved in 60 mL deionized water with concentrations of 20 mM and 75 mM respectively. After 30 min of vigorous stirring with Ar, 10 mL sodium hydroxide (NaOH) aqueous solution with 0.25 M was added dropwise to the above solution and continued stirring for another 15 min. The product was centrifuged, washed with deionized water and ethanol several times, and dried at 60 °C overnight under vacuum. The resulting blue powder was annealed at 200 °C for 2 h under atmosphere and the black CuO nanowires was obtained. In a typical synthesis of the Pd@CuO catalyst with 1.5 ± 1.0 nm Pd nanoparticles, 10 mg CuO nanowires were disperse evenly in 3 mL ethanol, then 1 mL of H_2PdCl_4 solution (2 mM in H_2O) were added and mixed with the CuO nanowires. After that, 1.2 mL of ascorbic acid (AA, 1 mM in H_2O) were rapidly added into the aforementioned solution with undisturbed condition for 20 min. The final product was collected by centrifugation and dried at 60 °C overnight under vacuum. The Pd nanoparticle without CuO support was synthesized with same method. The different size of Pd nanoparticles were synthesized by the change in concentration of H_2PdCl_4 (Table S2). The x in as-synthesized Pd_x @CuO means the concentration of H_2PdCl_4. The Pd@CuO catalyst (5 mg) and Nafion 117 solution (50 *u*L) were dispersed in ethanol (1 mL), and sonicated for 40 min. Then, the working electrode is prepared by drop casting the Pd@CuO suspension on the surface of carbon paper, which was pre-treated with nitric acid, acetone and deionized water. The catalyst loading was 1.0 ± 0.1 mg/cm^2 for Pd@CuO, Pd/C, and CuO.

2.3. Characterizations

X-ray photoelectron spectroscopy (XPS) was performed using a Thermo ESCALAB XI+ surface analysis system. Powder X-ray diffraction (XRD) data were acquired with a Bruker D8 Advance. Scanning electron microscope (SEM) images and energy dispersive X-ray (EDX) spectra were obtained with a HITACHI UHR FE-SEM SU8220 and JEOL JSM 7401 equipped with an EDX system. Transmission electron microscope (TEM) images were acquired using a JEOL JEM2100 instrument. Raman spectrum data were obtained with a Renishaw inVia Qontor. Infrared spectroscopy (IR) spectrum was conducted by Thermo Nicolet IS50. Ultraviolet and visible (UV–vis) spectrum was conducted by Shimadzu UV-3600 Plus. High performance liquid chromatography (HPLC) results were from Shimadzu LC-16.

2.4. Electrochemical measurements

The electrochemical behavior was carried out with a CH Instrument 660E potentiostat. The electrochemical cell contained the sample as a WE, a carbon rod as an auxiliary electrode, and Hg/HgO (1.0 M KOH, Aida) as a reference electrode ($E^{\circ}_{Hg/HgO}$ = 0.098 V vs. SHE). The electrolyte solution is 0.1 M KOH solution. The reference electrodes were calibrated by measuring the standard hydrogen electrode (SHE) potential. Potentials were converted to RHE via the Nernst equation: E_{RHE}

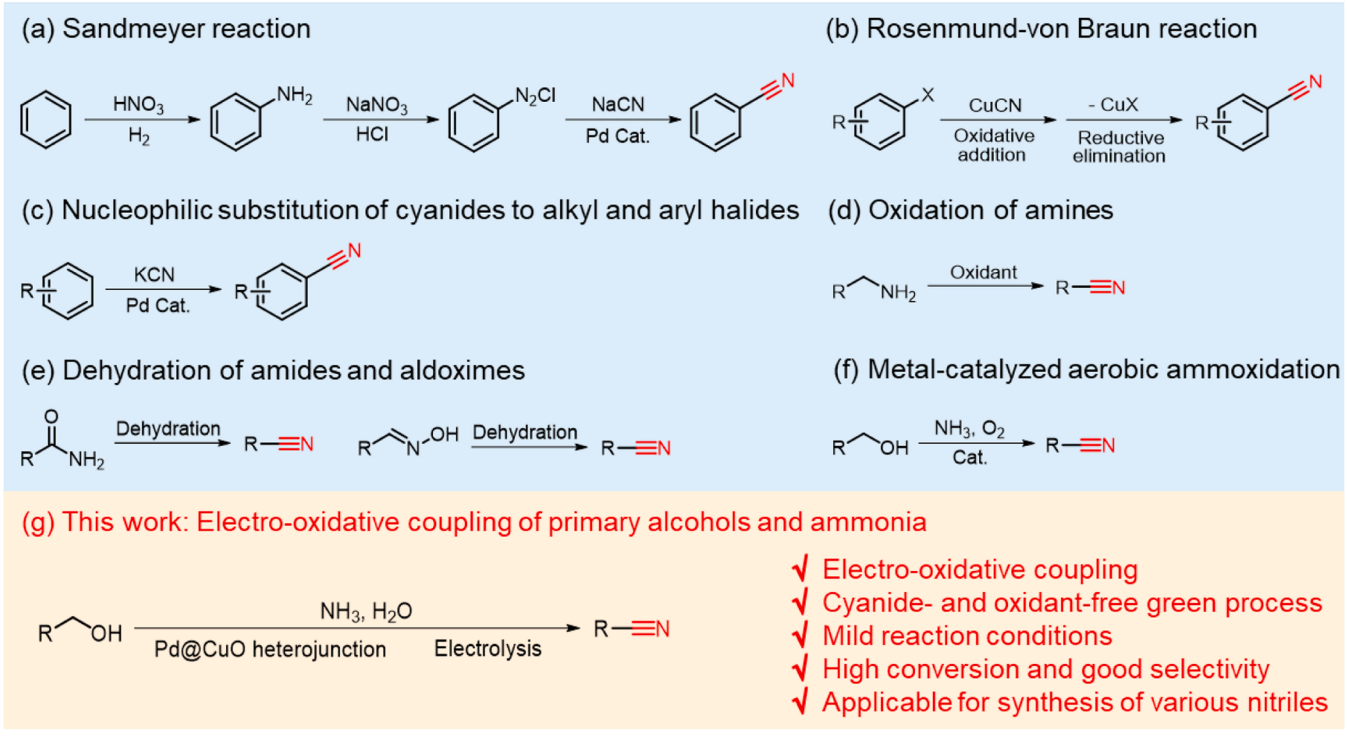

Scheme 1. Previously reported routes (a)–(f) and the route (g) developed in this work for nitrile synthesis.

$= E_{Hg/HgO} + 0.059 \times pH + E^{\circ}_{Hg/HgO}$. The chronoamperometry of benzyl alcohol (BA) and ammonia were conducted by the Pd@CuO catalyst as WE with electrode area of 5 cm^2 in 25 mL of electrolyte solution. In the experiment of isotope tracing, the water of ^{18}O (99.5 %) is used instead of ordinary water as the electrolyte solvent, and the $^{15}NH_3$ is used as the source of ammonia. The Faradaic efficiency values for the electrochemical coupling of BA and ammonia were calculated using the following equations (F, Faraday's constant, 96,485.33289 $\pm$ 0.00059 C mol^{-1}):

$$\text{FE of benzonitrile} = \frac{\text{mol of (benzonitrile + benzamide) formed}}{\text{Total charge passed}/(4 \times F)} \times 100\% \quad \text{(E1)}$$

$$\text{FE of benzaldehyde} = \frac{\text{mol of benzaldehyde formed}}{\text{Total charge passed}/(2 \times F)} \times 100\% \quad \text{(E2)}$$

$$\text{FE of benzoic acid} = \frac{\text{mol of benzoic acid formed}}{\text{Total charge passed}/(4 \times F)} \times 100\% \quad \text{(E3)}$$

$$\text{FE of nitrate} = \frac{\text{mol of nitrate formed}}{\text{Total charge passed}/(8 \times F)} \times 100\% \quad \text{(E4)}$$

Analysis of the coupling products of BA and ammonia were performed using a Shimadzu Prominence high performance liquid chromatography (HPLC) system equipped with an SPD-M20A diode array detector and a 4.6 mm × 150 mm Shim-pack GWS 5 μm C-18 column at 40 °C. HPLC eluents for the chronoamperometry of coupling products were mixtures of H_2O (0.1 % H_3PO_4) and CH_3CN with ratio of 4:6, and CH_3CN:H_2O = 6:4 for BA and its oxidation products. Wavelength for analysis: 280 nm. The oxidative product of ammonia was analyzed by ion chromatography (IC), and the gas product was determined by a Shimadzu Prominence gas chromatography (GC).

2.5. Computational details

All density functional theory (DFT) calculations in the work were carried out using the Vienna *ab initio* simulation program (VASP) [32,33]. The projector-augmented wave (PAW) method [33,34] was utilized to describe the core-valence interactions, and the plane-wave basis expansion cut-off energy was set to be 450 eV. For exchange and to correlate the functional, the generalized gradient approximation (GGA) was used with Perdew–Burke–Ernzerhof (PBE) [35] to perform all spin-polarized calculations. For the model construction, a $p(4 \times 2)$ CuO (111) surface and a $p(4 \times 4)$ Pd (111) surface with four-layers were modeled, in which the top two layers were allowed to fully relax and the bottom two layers were kept fixed to mimic the bulk region. To build the Pd cluster over the CuO surface, the ab-initio molecular dynamics (AIMD) was conducted at experimental temperature (300 K) for over 15 *ps* with a time step of 1 *fs*, where the last 5 *ps* energy profile was shown in Fig. S26. A ~20 Å vacuum layer was used to eliminate the interaction between neighboring slabs. The free molecules of NH_3, H_2 and C_7H_8O were placed in a (15 × 15 × 15) $Å^3$ cubic box to minimize the interaction of neighboring molecules. A 2 × 2 × 1 Monkhorst–Pack k-point mesh sampling was used for all optimizations. The equilibrium was reached when the forces on the relaxed atoms and the energies in the self-consistent iterations became less than 0.02 eV/Å and 10^{-5} eV, respectively. The van der Waal (vdW) interaction was described by the DFT-D3 method [36,37]. The transition states (TSs) were located with a constrained minimization technique [38–40] and the climbing image nudged elastic band (CI-NEB) method [41,42], with the forces on the relaxed atoms less than 0.05 eV $Å/^{-1}$. The Gibbs free energy can be expressed as:

$$\Delta G = \Delta E + \Delta ZPE - T\Delta S \quad \text{(E5)}$$

where ΔE is the reaction energy calculated by the DFT methods. ΔZPE and $T\Delta S$ are the thermodynamic corrections of zero-point-energy (ZPE) and entropy (S) derived from vibrational partition function at 298.15 K. As for gaseous species, the thermodynamic corrections were calculated using the Gaussian 03 software package with the ideal gas approximation.

3. Results and discussions

3.1. Characterization of palladium nanoparticles supported on CuO nanowires (Pd@CuO nanowires)

As shown in Fig. S1, the Pd@CuO catalyst displayed diffraction peaks of XRD at 40.01° and 46.53°, corresponding to the (111) and (200) planes of the Pd phase (JCPD card No. 88-2335). The other XRD peaks were consistent with CuO (JCPD card No. 72-0629). SEM images of the Pd@CuO nanowires indicated a length of 1–5 μm and a diameter of 80–100 nm (Figs. 1a and S2). TEM images showed that the Pd nanoparticles are modified on the surface of CuO nanowires with a size of approximately 1.5 ± 0.6 nm (Fig. 1b-c). The high-resolution TEM image of Pd@CuO showed lattice fringes with planar spacings of 0.223 and 0.232 nm, corresponding to the (111) planes of Pd and CuO (Fig. 1d). The selected area electron diffraction (SAED) pattern of Pd@CuO showed the polycrystalline structure and different crystal facets of Pd and CuO (inset in Fig. 1d). Elemental mapping images demonstrated that Cu and O are evenly distributed in the nanowires, while the Pd nanoparticles were uniformly dispersed on the surface of CuO nanowires (Fig. 1e-i). XPS survey spectrum suggested that Cu, O, and Pd are the primary elements in the as-prepared material (Fig. S3). The fitted Pd XPS spectrum (Fig. 1j) showed peaks at 335.23 and 340.56 eV, which are attributed to Pd^0 $3d_{5/2}$ and $3d_{3/2}$, respectively [43]. The Cu $2p_{3/2}$ XPS spectrum of Pd@CuO showed a peak at 934.27 eV, which is assigned to Cu^{2+} (Fig. 1k). This peak was slightly shifted compared to the corresponding peak of CuO (934.07 eV) (Fig. S4a), indicating that the surface Pd nanoparticles may affect the oxidation state of CuO. Furthermore, the O 1 *s* spectrum showed two distinct peaks at 529.87 and 531.76 eV, corresponding to lattice oxygen and surface-absorbed oxygen, respectively (Figs. 1l and S4b).

3.2. Electro-oxidative coupling of benzyl alcohol and NH_3

The electrocatalytic property of Pd@CuO toward the synthesis of nitrile was first investigated through a probe reaction, which involved the electrochemical synthesis of benzonitrile from benzyl alcohol (BA) and aqueous ammonia (Fig. 2a). First, the influences of the ammonia concentration and the applied potential on the electrochemical coupling reaction were explored with a constant concentration (10 mM) of BA. The highest selectivity of 83.2 % to benzonitrile (based on carbon containing products) was achieved in the electrolyte containing 2 M ammonia at 1.50 V versus reversible hydrogen electrode (vs. RHE) (Figs. 2b, S5, S6 and S7). With either an increase or a decrease of the ammonia concentration, the selectivity of benzonitrile declined. When Pd@CuO was replaced with CuO nanowires, the selectivity to benzonitrile decreased to 8.4 %, while the selectivity to benzoic acid increased to 82.0 % (Fig. S8). Chronoamperometric experiments using commercial Pd/C (10 wt%) nanoparticles as catalyst yielded neither benzonitrile nor BA oxidation products (Table S1). These contrasting results indicated that the unique catalytic activity of Pd@CuO is attributable to the synergistic effect of the Pd nanoparticles and CuO nanowires. The electrogenerated copper species with a high oxidation state may provide the driving force for the oxidant-free oxidation reactions, while Pd nanoparticles may promote the coupling reaction.

HPLC was used to monitor the product distribution in the Pd@CuO-catalyzed reaction. Figs. 2c and S9 show the changes in the concentrations of BA and its derivatives during the chronoamperometric test at 1.50 V vs. RHE with 2 M ammonia and 10 mM BA. Benzaldehyde, benzonitrile, and benzoic acid were detected by HPLC analysis in the

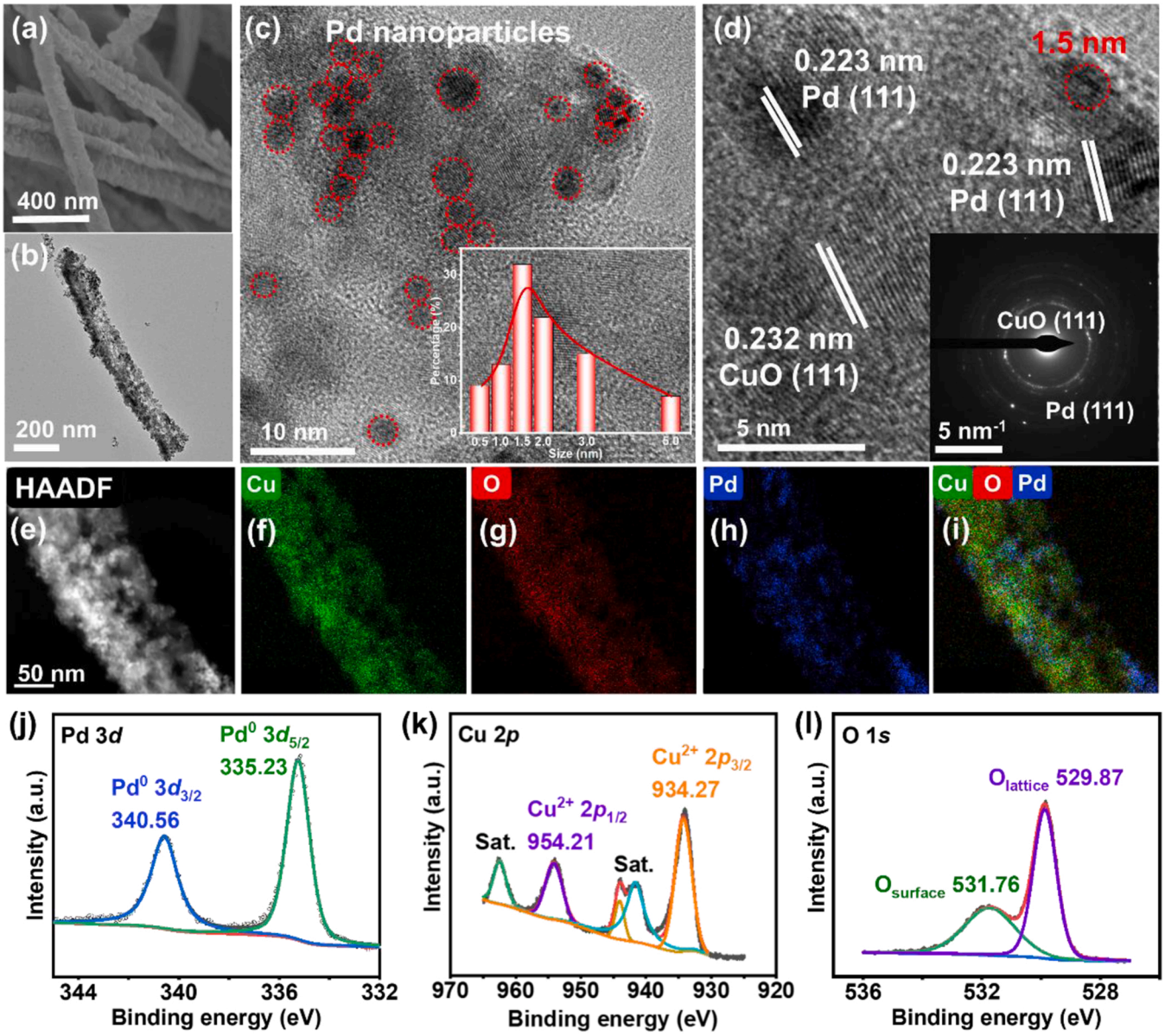

Fig. 1. Morphology and XPS spectra of the Pd@CuO catalyst. (a) SEM and (b,c) TEM images of Pd@CuO; the inset of (c) shows the size distribution of Pd nanoparticles. (d) High-resolution TEM image; the inset of (d) shows the SAED pattern of Pd@CuO. (e) HAADF-STEM image and (f-i) EDX elemental mappings of Pd@CuO. (j) Pd 3*d*, (k) Cu 2*p*, and (m) O 1 *s* XPS spectra of Pd@CuO.

first 30 min of the reaction, with relative concentrations of 28.1 %, 11.9 %, and 3.0 %, respectively. Thereafter, the content of benzonitrile continued to increase, accompanied by the formation of a small amount of benzoic acid, while the content of benzaldehyde decreased. After 4 h, when the passing charge reached 331.5 C, the conversion of BA was over 99.0 %, and the selectivities for benzonitrile, benzoic acid, benzamide, and benzoxazine were 83.2 %, 11.2 %, 4.0 %, and 1.6 %, respectively. Control experiments demonstrated that the detected benzamide is generated through the hydrolysis of benzonitrile under the electrolysis conditions (Fig. S10). Furthermore, chronoamperometric experiments using $H_2^{18}O$ and $^{15}NH_3$ demonstrated that benzonitrile, benzamide, and benzoxazine originate from the reaction of BA and ammonia, while benzoic acid originates from the oxidation of BA (Fig. 2d).

Water oxidation, BA oxidation, and ammonia oxidation are the major competitive reactions under experimental conditions. Linear sweep voltammetry (LSV) curves of Pd@CuO showed that the onset potential for water oxidation is 1.62 V vs. RHE, while BA and ammonia oxidation are initiated at around 1.40 V vs. RHE (Fig. S11). The chronoamperometric test at 1.35 V vs. RHE showed a faradic silence signal for the oxidation of BA or ammonia. When the applied potential was increased to 1.40 V vs. RHE, BA was oxidized to benzaldehyde (89.1 %) and benzoic acid (8.9 %) (Fig. S12a). The yield of benzoic acid increased with further enhancing the applied potential, reaching up to 99.0 % at 1.60 V vs. RHE. The chronoamperometric tests at potentials from 1.40 to 1.60 V vs. RHE in the presence of ammonia showed that nitrate is the major oxidation product (Figs. S12b and S13) [44]. Meanwhile, a small amount of hydrazine was detected as an intermediate using the Watt and Chrisp method (Figs. S14 and S15) [45].

3.3. Mechanism of the electro-oxidative coupling on the surface of Pd@CuO

The Pd nanoparticle with a size of 1.5 ± 0.6 nm was prepared without CuO as support, and the Pd $3d_{3/2}$ binding energy shifts by 0.37 eV compared with Pd@CuO (Fig. S16), which indicating the successful construction of the Pd/CuO heterojunction [46,47]. The

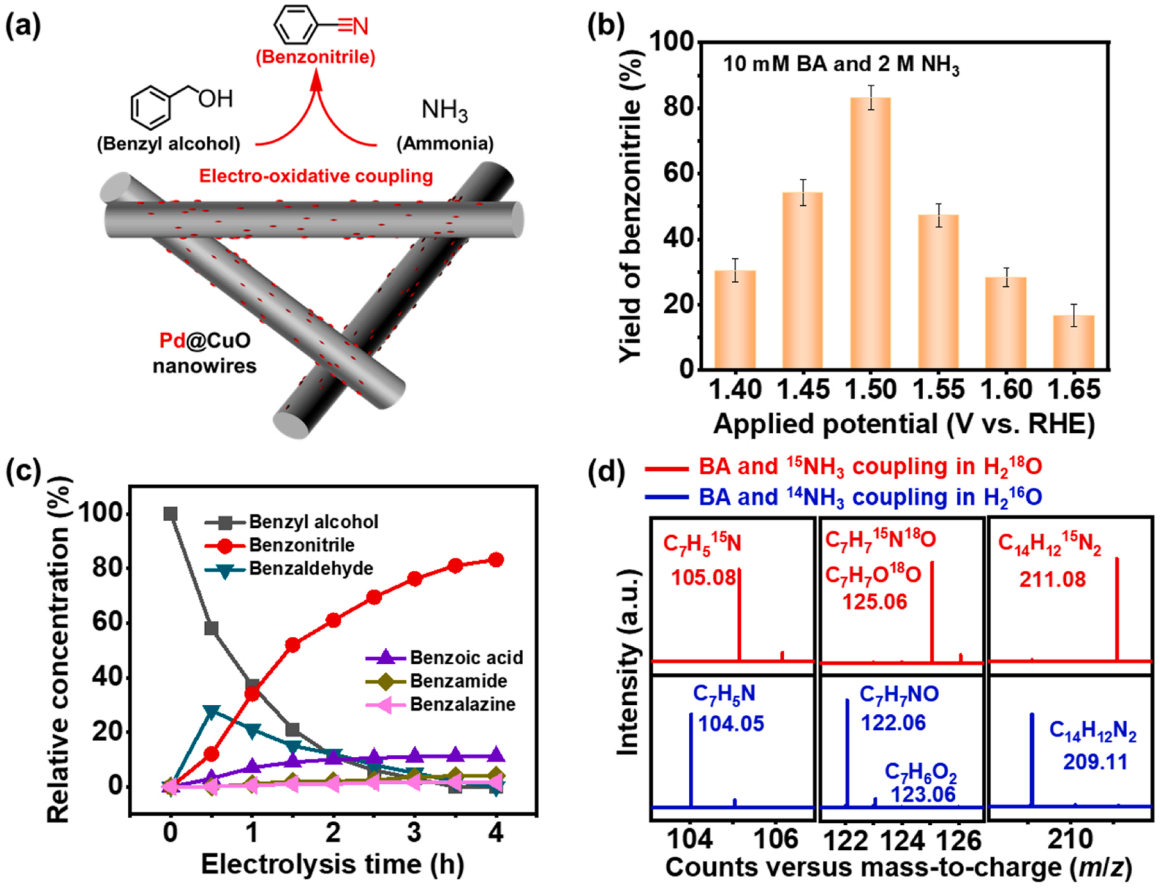

Fig. 2. Evaluation of the electrocatalytic performance of the Pd@CuO catalyst toward nitrile synthesis. (a) Schematic diagram for benzonitrile synthesis. (b) Benzonitrile generation by electro-oxidative coupling of benzoyl alcohol in the presence of ammonia. (c) Chronoamperometric test at 1.50 V vs. RHE for the reaction of 10 mM benzoyl alcohol and 2 M ammonia. (d) Mass spectra of the products (benzonitrile, benzoic acid, benzamide, and benzoxazine) obtained from the reactions using unlabeled and isotope-labeled substrates.

importance of the heterojunction in Pd@CuO was investigated by tailoring the size of Pd nanoparticles. Generally, a decrease in the size of Pd nanoparticles indicates an increased Pd/CuO heterojunction. The size of Pd nanoparticles was controlled by adjusting the added amount of H_2PdCl_4 during the preparation process. Consequently, Pd nanoparticles with sizes of 5.0 ± 1.1, 3.0 ± 0.9, and 1.5 ± 0.6 nm were prepared and modified on the CuO nanowires (Fig. S17). XPS analysis showed that the Pd $3d_{3/2}$ binding energy gradually shifts by 0.31 eV toward higher energies as the Pd particle size decreases from 5.0 ± 1.1–1.5 ± 0.6 nm (Fig. S18a). A further decrease in the added amount of H_2PdCl_4, only lowered the Pd content in Pd@CuO, the size of the Pd nanoparticles remained around 1.5 ± 0.6 nm, and Pd $3d_{3/2}$ binding energy did not display further shift. These results indicated that 1.5 ± 0.6 nm is the limiting size for Pd nanoparticles. As the size of Pd nanoparticles decreased from 5.0 ± 1.1–1.5 ± 0.6 nm, along with a decrease in the amount of supported Pd and an increase in Pd/CuO heterojunction (Table S2), the selectivity toward benzonitrile went up from 71.3 % to 83.2 % under the same catalytic conditions and the same loading amount of Pd@CuO (1.0 ± 0.1 mg/cm^2) (Fig. S18b). Furthermore, a decrease in the content of the supported Pd from 1.46 to 1.21 wt%, with the loading amount of Pd@CuO (1.0 ± 0.1 mg/cm^2) and the Pd nanoparticle size (1.5 ± 0.6 nm) being kept constant, could lead to the decrease of heterojunction, which resulted in a decrease in the selectivity of benzonitrile from 83.2 % to 78.1 %. All these results suggested that the Pd/CuO heterojunction plays an important role in the electrochemical synthesis of nitriles.

X-ray absorption spectroscopy is used to examine the atomic contact property of Pd@CuO (Fig. S19 and Table S3). As shown in Fig. S19, the extend X-ray absorption fine structure signals of Pd@CuO are different from the reference CuO. Pd@CuO shows two types of space-occupying Cu-O sites, the total coordination number of Cu-O is about three. Furthermore, Cu-O-Cu and Cu-O-Pd signals can be detected on the shell layer. These extend X-ray absorption fine structure results indicated a strong interaction between the Pd nanoparticles and the CuO, attributed to the heterogeneous structure.

To gain insight into the mechanism of the electrochemical synthesis of nitriles from primary alcohols and ammonia over Pd@CuO, electrochemical in situ Raman spectroscopy (ISRS) and open circuit potential (OCP)-time technology were employed to trace the formation of high-valence metal species and to monitor their lifetimes. In the absence of benzyl alcohol and ammonia, no discernible change was observed in the ISRS spectra of pristine Pd@CuO at potentials ≤ 1.35 V vs. RHE; peaks at 291, 341, and 630 cm^{-1} were attributed to the Cu-O vibrations of CuO [48,49]. A new Raman band at 581 cm^{-1} began to appear at the applied potential of 1.40 V vs. RHE, and the intensity of the band gradually increased with the applied potential being enhanced from 1.40 to 1.60 V vs. RHE, which indicated the formation of Cu^{III} species (Fig. 3a). This observations were similar to that of the CuO reference in its ISRS spectra (Fig. S20). However, Pd kept intact in the potential range of 1.40–1.60 V vs. RHE. Upon the addition of BA and NH_3, the band at 581 cm^{-1} was diminished, indicating that the Cu^{III} species was reduced in the BA and NH_3 system. The electrogenerated Cu^{III} species on Pd@CuO displayed an E_{OCP} value of 1.40 V vs. RHE (Fig. 3b), which went down spontaneously to 0.85 V vs. RHE, indicating the conversion of Cu^{III} to Cu^{II} species with a lifetime of ~7000 s. By contrast, the lifetime of Cu^{III} was shortened to ~200 s upon the addition of BA and NH_3

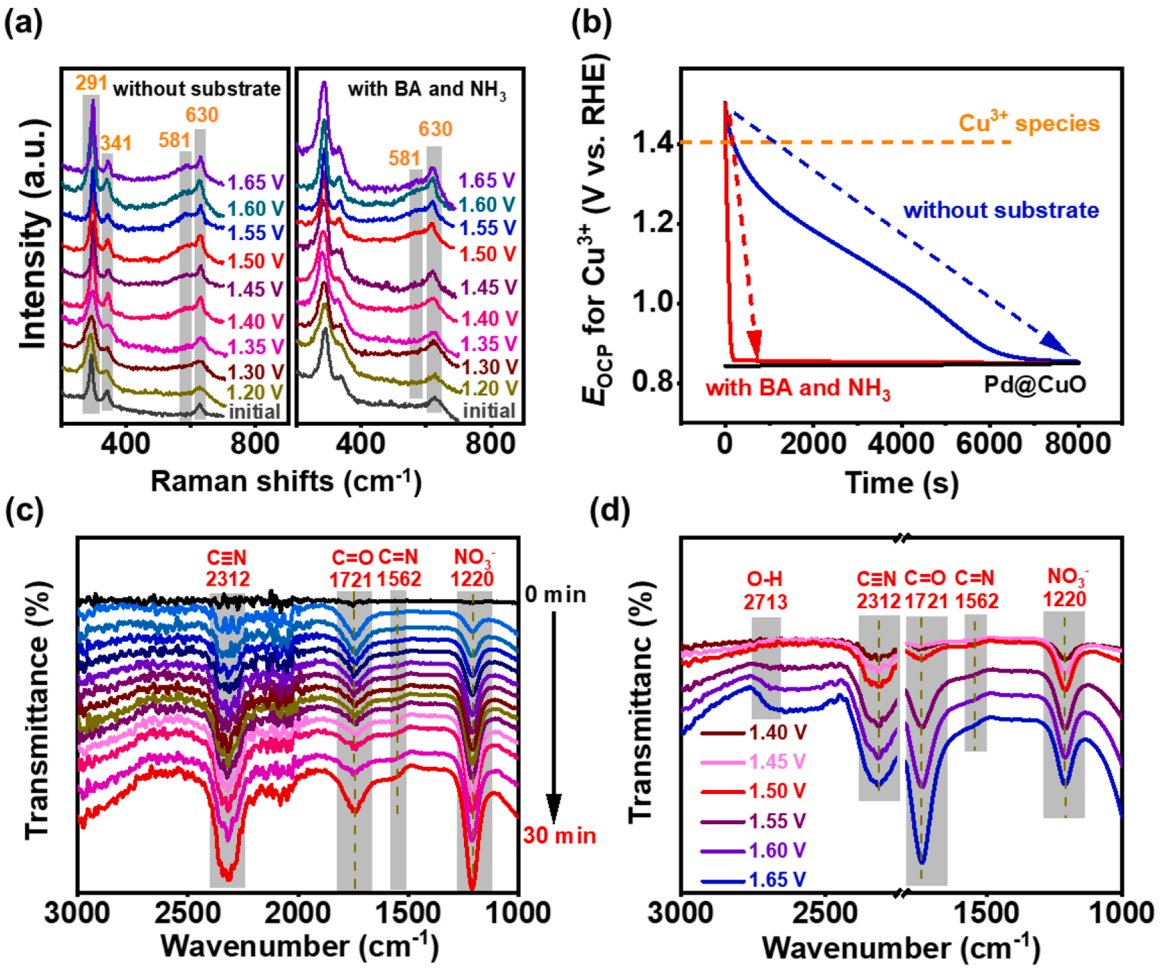

Fig. 3. In situ electrochemical analysis to evaluate the reaction. (a) Raman absorptions of the Pd@CuO electrode interface in the presence and absence of BA and NH3 after being used for the electrocoupling at various potentials. (b) Open circuit voltage-time tests on the surface of the Pd@CuO electrode. (c) Infrared spectra of the Pd@CuO electrode interface measured by monitoring the electrochemical reaction process at 1.50 V vs. RHE in the 0.1 M KOH solution containing 10 mM benzyl alcohol and 2 M ammonia. (d) Infrared spectra of the Pd@CuO electrode interface after being used for the electrochemical test at a set potential for 30 min.

(Fig. 3b). Similar behaviors are observed when BA is replaced by alkyl alcohol (1-pentanol) (more details, see Supporting Note 1).

These results indicated that the Cu^{II} species on Pd@CuO are first oxidized to Cu^{III} species, and these electrogenerated Cu^{III} species provide the driving force for oxidation reactions. Moreover, control experiments using the CuO electrode showed a higher E_{OCP} value (0.90 V vs. RHE) and shorter lifetime (~2000 s) of the electrogenerated Cu^{III} species (Fig. S21), suggesting that CuO is the oxidative active center, and the surface Pd nanoparticles could tune the oxidation state of CuO.

To gain further insight into the formation of benzonitrile over Pd@CuO, the catalytic processes at different applied potentials were monitored by in-situ electrochemical Fourier transform infrared (IEFT-IR) spectroscopy. The absorption bands at around 1220, 1562, 1721, and 2312 cm^{-1} in IEFT-IR spectra (Fig. 3c, S22 and S23) were assigned to the stretching vibrations of NO_3^-, C═N, C═O, and C≡N, respectively. In the first 30 min, the absorption strength of NO_3^- and C≡N increased linearly with time, while the bands of C═N and C═O reached a steady-state strength within 5 min and remained constant for the next 25 min (Fig. S24). These results indicated that some C═O and C═N species are probable intermediates that are consumed rapidly in subsequent steps. When the applied potential reached 1.55 V vs. RHE (Fig. 3d), a considerable amount of benzoic acid was formed showing that a higher potential will facilitate the formation of by-product and decline the yield of nitrile compound.

The possible reaction pathways for the electro-oxidative coupling of benzyl alcohol and ammonia are proposed in Fig. S25. More evidence on the reaction pathways and reactive intermediates are investigated through controlled experiments (Fig. S26). A selectivity of 61.5 % for benzonitrile is obtained with benzaldehyde and NH_3 as reactants, indicating that the first step intermediate is benzaldehyde. Controlled experiments using H_2N-NH_2 to replace NH_3 achieve substantial benzonitrile, demonstrating that both H_2N-NH_2 and NH_3 are possible nitrogen sources. However, no benzonitrile is detected without the anodic conditions, indicating that the anodic-activated H_2N * is the real intermediate for the coupling step. Based on the HPLC and IEFT-IR results, phenylmethanimine, benzamide, and benzoxazine are possible coupling intermediates. A controlled experiment with benzamide and benzoxazine as reactants, respectively, achieved no benzonitrile, certifying these two pathways are impracticable. Phenylmethanimine is a feasible intermediate for benzonitrile production, which has been reported in the benzylamine dehydrogenation research works [50]. Unfortunately, we cannot prove this step through controlled experiments, due to the unstable property of phenylmethanimine.

Based on the above experimental evidences and previously reported results [51,52], the possible mechanism for the electro-oxidative coupling of benzyl alcohol and ammonia over Pd@CuO catalyst was proposed in Fig. 4a. First, Cu^{2+} species on Pd@CuO were oxidized to $Cu^{3+}OH$, which acted as an in-situ-generated renewable oxidant and was consumed for further reactions. Afterward, benzyl alcohol occured two successive dehydrogen steps to form benzaldehyde (**D**) on the

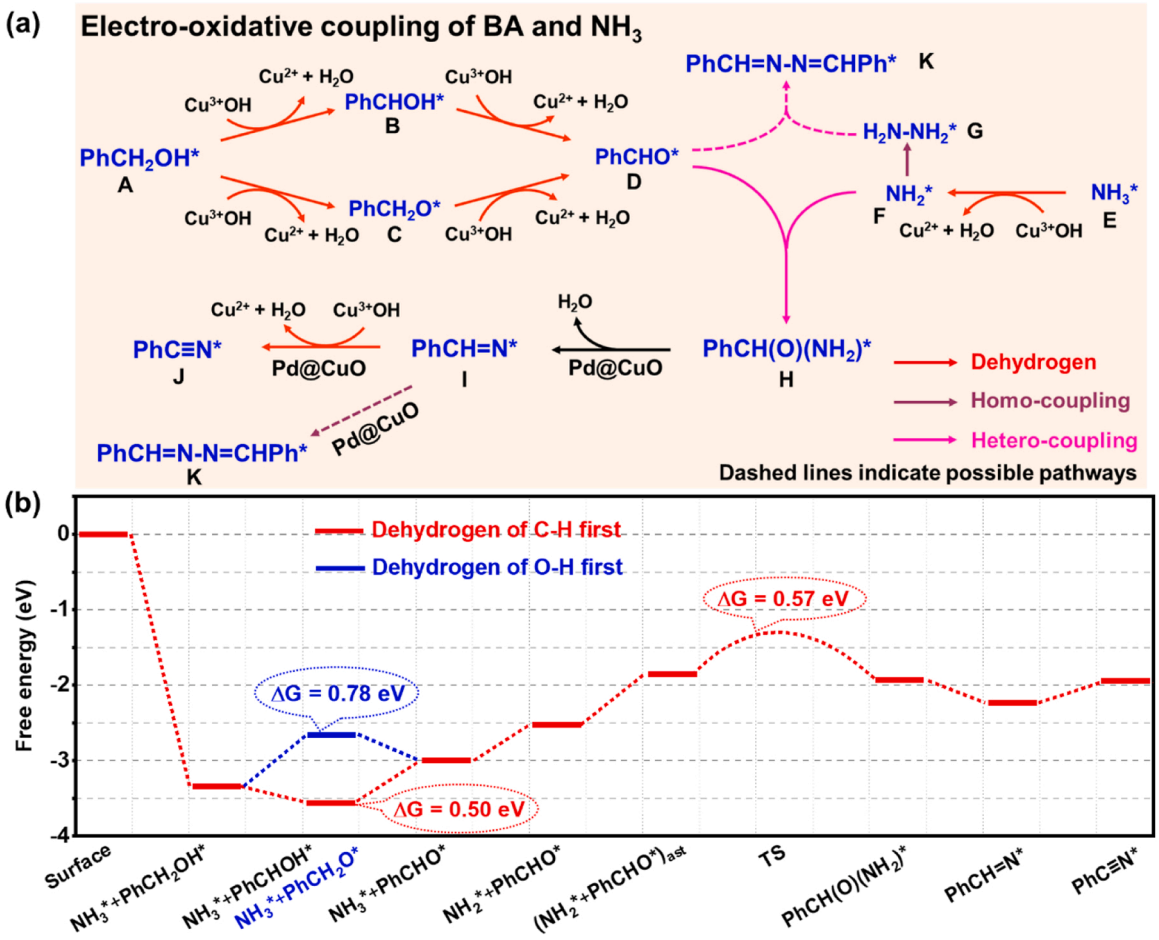

Fig. 4. Possible mechanism and related theoretical calculation results for the electro-oxidative coupling reaction of benzyl alcohol and ammonia. (a) The plausible electrochemical mechanism for the synthesis of benzonitrile. (b) Free energy diagram for the reaction of benzyl alcohol and ammonia on Pd@CuO.

Pd@CuO surface. Notably, there were two sequences for the homolytic cleavage of benzylic C-H and O-H bonds to form benzaldehyde: one with breaking C-H before the cleavage of O-H through intermediate **B**, and the other with breaking C-H after the cleavage of O-H through intermediate **C**. These forward steps were driven by the electrogenerated $Cu^{3+}OH$ species via base catalysis, which had been theoretically suggested and experimentally identified on anodic catalyst surfaces during the alkaline oxygen evolution reaction [53–60]. Meanwhile, one of the N-H bonds of NH_3 homolytically cleaves to form **F** on Pd@CuO. Subsequently, the two intermediates, **D** and **F**, took place in a coupling reaction (hetero-coupling) on the catalyst surface, and the resulting intermediate **H** was further dehydrated to form an imine-N intermediate **I**. Finally, benzonitrile (**J**) was formed by further break of the benzylic C-H bond of **I**, and the by-product **K** was generated via a homo-coupling reaction of **I** or hetero-coupling of **D** and **G**. Meanwhile, H_2 was simultaneously produced at the cathode via the hydrogen evolution reaction (HER).

DFT calculations were performed to further investigate the thermodynamic feasibility of the mechanism. The results were shown in Fig. 4b. The stable Pd@CuO heterojunction structure was built by AIMD (Fig. S27). Analysis of the charge density difference showed that electrons are transferred from Pd to CuO (Fig. S28). Higher-valence Pd species were more conducive to the oxidation reaction, while the transfer of electrons to Cu was more conducive to maintaining Cu at + 3 oxidation state rather than transforming it to an unstable higher valence state. This inference from the calculations was consistent with the experimental results of the OCP-time analysis (Fig. 3b). According to the calculated absorption energies of ammonia and benzyl alcohol on the surface of Pd@CuO (Fig. S29), benzyl alcohol was more strongly adsorbed compared to ammonia, which signified that the absorption of benzyl alcohol on the Pd@CuO surface is the initial step for the production of benzonitrile. The corresponding reaction models are shown in Fig. S30.

Fig. 4b and S31 showed that the dehydrogen pathway on the Pd@CuO surface occurs preferably at the benzylic C-H, with an activation barrier (ΔG_a) of 0.50 eV, which was lower than the initial activation barrier (0.78 eV) for the O-H of benzyl alcohol. Furthermore, the second dehydrogenation occured at the O-H site with an activation barrier of 0.06 eV rather than C-H bond cleavage (activation barrier of 0.68 eV), leading to the production of benzaldehyde. Then, the absorbed ammonia was deprotonated to generate NH_2 * with a reaction barrier of 0.49 eV. Before the coupling of Ph-CHO* and NH_2 *, adsorption occured completely on Pd, while adsorption occured on heterojunction after the coupling (ΔG = 0.23 eV; Fig. S32). The Gibbs free energy of activation for the coupling of Ph-CHO* and NH_2 * on the surface of Pd@CuO was 0.57 eV, and this was the rate-determining step for the entire reaction. Compared to that on the Pd@CuO heterojunction, the C-N coupling barrier on CuO was 0.66 eV (Fig. S33), resulting in a much lower yield of benzonitrile (Fig. S7). The coupling product PhCH(O)(NH_2) * spontaneously underwent rapid dehydration to produce intermediate PhCH=N * . Finally, PhCN* was formed by further dehydrogen of PhCH=N * .

3.4. Substrate scope investigation

The general applicability of this strategy for nitrile synthesis by the

electro-oxidative coupling of primary alcohols and ammonia was investigated by using various primary alcohols with aromatic groups (**1–22**), heterocyclic aromatic groups (**23–25**), as well as cyclic and liner alkyl groups (**26–33**) (Scheme 2). Encouragingly, good conversions (80–99 %) of all tested primary monoalcohols and satisfactory yields (65.3–83.2 %) of nitriles were obtained. When 1,4-butanediol was used as starting compound, the succinonitrile was produced in a yield of 54.1 %. These results showed the general applicability of this method for green synthesis of various nitriles.

4. Conclusion

A new method was developed for the green synthesis of nitriles by electro-oxidative coupling of primary alcohols and aqueous ammonia under mild conditions. With Pd@CuO as an anodic electrode, the electro-oxidative coupling of benzyl alcohol and ammonia at 1.50 V vs. RHE afforded a good yield of 83.2 % for benzonitrile. Such a facile synthetic method had been demonstrated to be applicable for the conversion of various primary alcohols to corresponding nitriles, giving yields of 65.3–83.2 % to nitriles for the reaction of tested primary monoalcohols with ammonia under optimal conditions. On the basis of

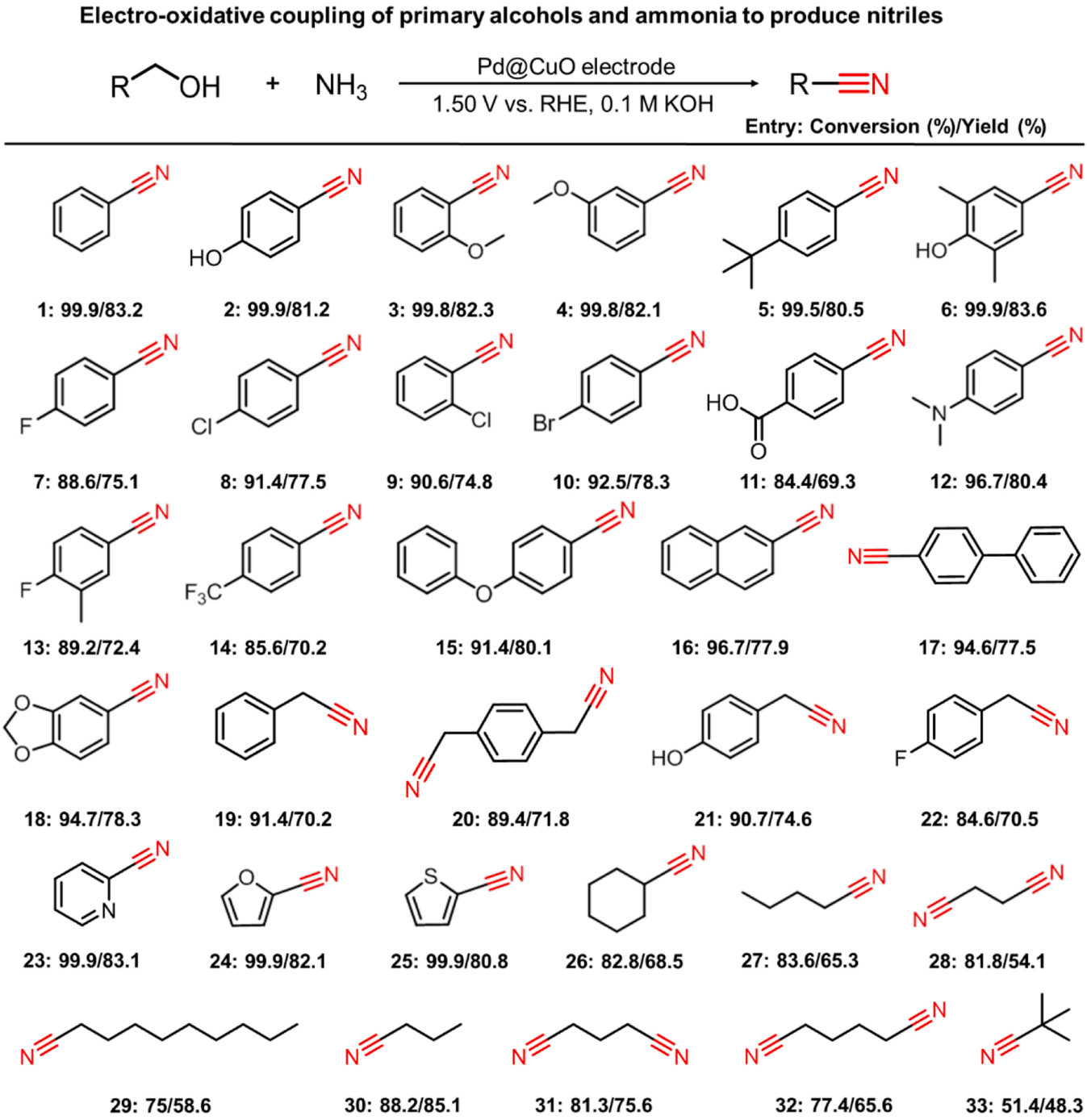

Scheme 2. Substrate scope of the electro-oxidative coupling of various primary alcohols and ammonia to synthesize nitriles over the Pd@CuO anode. Reaction conditions: primary alcohols (10 mM), ammonia (2 M), Pd@CuO (working area: 4 cm^2), 0.1 M KOH, at an applied potential of 1.50 V vs. RHE at 25 °C. Products and yields are determined by NMR and HPLC analyses.

experimental evidence and calculation results, demonstrated that the synergistic effect of CuO and Pd induces the catalytic reaction. The unique catalytic performance of Pd@CuO was attributed to the synergistic effect of Pd nanoparticles and CuO nanowires. Specifically, the electrogenerated Cu^{3+} species on the surface of CuO nanowires may act as the active center for the electrochemical oxidation of substrates, while the Pd nanoparticles stabilized the Cu^{3+} species and reduce the Gibbs energy barrier of the coupling reaction. The results of this work provided an environment-friendly, low-cost and convenient approach for the production of nitriles.

CRediT authorship contribution statement

Z. F. designed the experiments, fabricated and analyzed the devices, carried out the TEM characterization, carried out, and analyzed the XPS measurements. **Y. D.** contributed to the density functional theory calculations, revision, and discussion of the paper. **L. W.** carried out the TEM characterization, **M. W., F. L., K. F.**, and **X. W.** contributed to the revision and discussion of the paper. **L.S.** supervised the project and contributed to the revision and discussion of the paper. **P. Z.** designed the experiments, supervised the project, and wrote the paper.

Declaration of Competing Interest

The authors declare that they have no known competing financial interests or personal relationships that could have appeared to influence the work reported in this paper.

Data availability

Data will be made available on request.

Acknowledgements

This work was financially supported by the National Natural Science Foundation of China (Nos. 21978040, 22088102), and National Key R&D Program of China (2022YFA0911900), the Fundamental Research Funds for the Central Universities (DUT22QN213). The authors thank Westlake university instrumentation and service center for physical sciences, Westlake center for micro/nano fabrication, Westlake university supercomputer center for the facility support and technical assistance. We also acknowledge technical support from Shanghai Synchrotron Radiation Facility.

Appendix A. Supporting information

Supplementary data associated with this article can be found in the online version at doi:10.1016/j.apcatb.2023.122999.

References

[1] A. Kleemann, J. Engel, B. Kutscher, D. Reichert. Pharmaceutical Substance: Synthesis Patents, Applications, fourth ed., Georg Thieme, Stuttgart, 2001.
[2] J.S. Miller, J.L. Manson, Designer magnets containing cyanides and nitriles, Acc. Chem. Res. 34 (2001) 563–570.
[3] F.F. Fleming, Q. Wang, Unsaturated nitriles: conjugate additions of carbon nucleophiles to a recalcitrant class of acceptors, Chem. Rev. 103 (2003) 2035–2078.
[4] J. Kim, H.J. Kim, S. Chang, Synthesis of aromatic nitriles using nonmetallic cyano-group sources, Angew. Chem. Int. Ed. 51 (2012) 11948–11959.
[5] Z. Rappoport, Chemistry of the Cyano Group, Wiley, London, 1970.
[6] R.C. Larock, Comprehensive organic transformations: a guide to functional group preparations, VCH, New York, 1989.
[7] H.H. Hodgson, The Sandmeyer reaction, Chem. Rev. 40 (1947) 251–277.
[8] C. Galli, Radical reactions of arenediazonium ions: an easy entry into the chemistry of the aryl radical, Chem. Rev. 88 (1988) 765–792.
[9] J. Lindley, Copper assisted nucleophilic substitution of aryl halogen, Tetrahedron 40 (1984) 1433–1456.
[10] H.-J. Cristau, A. Ouali, J.-F. Spindler, M. Taillefer, Mild and efficient copper-catalyzed cyanation of aryl iodides and bromides, Chem. Eur. J. 11 (2005) 2483–2492.
[11] J. Zanon, A. Klapars, S.L. Buchwald, Copper-catalyzed domino halide exchange-cyanation of aryl bromides, J. Am. Chem. Soc. 125 (2003) 2890–2891.
[12] M. Sundermeier, S. Mutyala, A. Zapf, A. Spannenberg, M. Beller, A convenient and efficient procedure for the palladium-catalyzed cyanation of aryl halides using trimethylsilylcyanide, J. Organomet. Chem. 684 (2003) 50–55.
[13] T. Schareina, A. Zapf, W. Mägerlein, N. Müllerb, M. Beller, A new palladium catalyst system for the cyanation of aryl chlorides with $K_4[Fe(CN)_6]$, Tetrahedron Lett. 48 (2007) 1087–1090.
[14] P. Anbarasan, T. Schareina, M. Beller, Recent developments and perspectives in palladium-catalyzed cyanation of aryl halides: synthesis of benzonitriles, Chem. Soc. Rev. 40 (2011) 5049–5067.
[15] F.G. Buono, R. Chidambaram, R.H. Mueller, R.E. Waltermire, Insights into palladium-catalyzed cyanation of bromobenzene: additive effects on the rate-limiting step, Org. Lett. 10 (2008) 5325–5328.
[16] D. Maiti, G.K. Lahiri, R. Ray, A.S. Hazari, Ruthenium catalyzed aerobic oxidation of amines, Chem. Asian J. 13 (2018) 2138–2148.
[17] R. Ray, S. Chandra, V. Yadav, P. Mondal, D. Maiti, G. Kumar Lahiri, Ligand controlled switchable selectivity in ruthenium catalyzed aerobic oxidation of primary amines, Chem. Commun. 53 (2017) 4006–4009.
[18] Z. Chen, W. Chen, L. Zhang, W. Fu, G. Cai, A. Zheng, T. Tang, Acidic hierarchical porous ZSM-5 assembled palladium catalyst: a green substitute to transform primary amides to nitriles, Appl. Catal. B 302 (2022), 120835.
[19] A. Rapeyko, M.J. Climent, A. Corma, P. Concepcion, S. Iborra, Nanocrystalline CeO2 as a highly active and selective catalyst for the dehydration of aldoximes to nitriles and one-pot synthesis of amides and esters, ACS Catal. 6 (2016) 4564–4575.
[20] J. Vilím, T. Knaus, F.G. Mutti, Catalytic promiscuity of galactose oxidase: a mild synthesis of nitriles from alcohols, air, and ammonia, Angew. Chem. Int. Ed. 57 (2018) 14240–14244.
[21] P. Han, C. Tang, S. Sarina, E.R. Waclawik, A. Du, S.E. Bottle, Y. Fang, Y. Huang, K. Li, H.-Y. Zhu, Wavelength-specific product desorption as a key to raising nitrile yield of primary alcohol ammoxidation over illuminated Pd nanoparticles, ACS Catal. 12 (2022) 2280–2289.
[22] W. Yin, C. Wang, Y. Huang, Highly practical synthesis of nitriles and heterocycles from alcohols under mild conditions by aerobic double dehydrogenative catalysis, Org. Lett. 15 (2013) 1850–1853.
[23] T. Oishi, K. Yamaguchi, N. Mizuno, Catalytic oxidative synthesis of nitriles directly from primary alcohols and ammonia, Angew. Chem. Int. Ed. 48 (2009) 6286–6288.
[24] R.V. Jagadeesh, H. Junge, M. Beller, Green synthesis of nitriles using non-noble metal oxides-based nanocatalysts, Nat. Commun. 5 (2014) 4123.
[25] L. Wang, G. Wang, J. Zhang, C. Bian, X. Meng, F.-S. Xiao, Controllable cyanation of carbon-hydrogen bonds by zeolite crystals over manganese oxide catalyst, Nat. Commun. 8 (2017) 15240.
[26] C. Liebig, S. Paul, B. Katryniok, C. Guillon, J.-L. Couturier, J.-L. Dubois, F. Dumeignil, W.F. Hoelderich, Glycerol conversion to acrylonitrile by consecutive dehydration over WO_3/TiO_2 and ammoxidation over Sb-(Fe,V)-O, Appl. Catal. B 132 (2013) 170–182.
[27] Y. Wang, S. Furukawa, N. Yan, Identification of an active NiCu catalyst for nitrile synthesis from alcohol, ACS Catal. 9 (2019) 6681–6691.
[28] A. Martin, N.V. Kalevaru, B. Lücke, J. Sans, Eco-friendly synthesis of p-nitrobenzonitrile by heterogeneously catalysed gas phase ammoxidation, Green. Chem. 4 (2002) 481–485.
[29] F. Yan, J.-F. Bai, Y. Dong, S. Liu, C. Li, C.-X. Du, Y. Li, Catalytic Cyanation of C−N Bonds with CO_2/NH_3, JACS Au 2 (2022) 2522–2528.
[30] H. Wang, Q. Luo, L. Wang, Y. Hui, Y. Qin, L. Song, F.-S. Xiao, Product selectivity controlled by manganese oxide crystals in catalytic ammoxidation, Chin. J. Cat. 42 (2021) 2164–2172.
[31] A.G.M. da Silva, T.S. Rodrigues, A.A. Parussulo, E.G. Candido, R.S. Geonmonond, H.F. Brito, H.E. Toma, Pedro H.C. Camargo, Controlled synthesis of nanomaterials at the undergraduate laboratory: $Cu(OH)_2$ and CuO nanowires, J. Chem. Educ. 94 (2017) 743–750.
[32] G. Kresse, J. Furthmüller, Efficient iterative schemes for ab initio total-energy calculations using a plane-wave basis set, Phys. Rev. B 54 (1996) 11169–11186.
[33] G. Kresse, D. Joubert, From ultrasoft pseudopotentials to the projector augmented-wave method, Phys. Rev. B 59 (1999) 1758–1775.
[34] P.E. Blöchl, Projector augmented-wave method, Phys. Rev. B 50 (1994) 17953–17979.
[35] J.P. Perdew, K. Burke, M. Ernzerhof, Generalized gradient approximation made simple, Phys. Rev. Lett. 77 (1996) 3865–3868.
[36] S. Grimme, J. Antony, S. Ehrlich, H. Krieg, A consistent and accurate ab initio parametrization of density functional dispersion correction (DFT-D) for the 94 elements H-Pu, J. Chem. Phys. 132 (2010), 154104.
[37] S. Grimme, S. Ehrlich, L. Goerigk, Effect of the damping function in dispersion corrected density functional theory, J. Comput. Chem. 32 (2011) 1456–1465.
[38] A. Alavi, P. Hu, T. Deutsch, P.L. Silvestrelli, J. Hutter, CO oxidation on Pt(111): an ab initiodensity functional theory study, Phys. Rev. Lett. 80 (1998) 3650–3653.
[39] A. Michaelides, P. Hu, Catalytic water formation on platinum: a first-principles study, J. Am. Chem. Soc. 123 (2001) 4235–4242.
[40] Z.P. Liu, P. Hu, General rules for predicting where a catalytic reaction should occur on metal surfaces: a density functional theory study of C-H and C-O bond breaking/making on flat, stepped, and kinked metal surfaces, J. Am. Chem. Soc. 125 (2003) 1958–1967.

[41] G. Henkelman, H. Jónsson, Improved tangent estimate in the nudged elastic band method for finding minimum energy paths and saddle points, J. Chem. Phys. 113 (2000) 9978–9985.
[42] G. Henkelman, B.P. Uberuaga, H. Jónsson, A climbing image nudged elastic band method for finding saddle points and minimum energy paths, J. Chem. Phys. 113 (2000) 9901–9904.
[43] C. Chen, X. Zhu, X. We, Y. Zhou, L. Zhou, H. Li, L. Tao, Q. Li, S. Du, T. Liu, D. Yan, C. Xie, Y. Zou, Y. Wang, R. Chen, J. Huo, Y. Li, J. Cheng, H. Su, X. Zhao, W. Cheng, Q. Liu, H. Lin, J. Luo, J. Chen, M. Dong, K. Cheng, C. Li, S. Wang, Coupling N_2 and CO_2 in H_2O to synthesize urea under ambient conditions, Nat. Chem. 12 (2020) 717–724.
[44] Y. Wang, C. Wang, M. Li, Y. Yu, B. Zhang, Nitrate electroreduction: mechanism insight, in situ characterization, performance evaluation, and challenges, Chem. Soc. Rev. 50 (2021) 6720–6733.
[45] Z. Geng, Y. Liu, X. Kong, P. Li, K. Li, Z. Liu, J. Du, M. Shu, R. Si, J. Zeng, Achieving a record-high yield rate of 120.9 μg_{NH3} mg-1cat. H^{-1} for N_2 electrochemical reduction over Ru single-atom catalysts, Adv. Mater. 30 (2018), 1803498.
[46] K. Wang, S. Shu, M. Chen, J. Li, K. Zhou, J. Pan, X. Wang, X. Li, J. Sheng, F. Dong, G. Jiang, Pd-TiO_2 Schottky heterojunction catalyst boost the electrocatalytic hydrodechlorination reaction, Chem. Eng. J. 381 (2020), 122673.
[47] Z. Li, M. Hu, P. Wang, J. Liu, J. Yao, C. Li, Heterojunction catalyst in electrocatalytic water splitting, Coord. Chem. Rev. 439 (2021), 213953.
[48] L. Debbichi, M.C. Marco de Lucas, J.F. Pierson, P. Krüger, Vibrational properties of CuO and Cu_4O_3 from first-principles calculations, and Raman and Infrared spectroscopy, J. Phys. Chem. C 116 (2012) 10232–10237.
[49] J.F. Xu, W. Ji, Z.X. Shen, W.S. Li, S.H. Tang, X.R. Ye, D.Z. Jia, X.Q. Xin, Raman spectra of CuO nanocrystals, J. Raman Spectrosc. 30 (1999) 413–415.
[50] Y. Sun, H. Shin, F. Wang, B. Tian, C.-W. Chiang, S. Liu, X. Li, Y. Wang, L. Tang, W. A. Goddard, M. Ding, Highly selective electrocatalytic oxidation of amines to nitriles assisted by water oxidation on metal-doped α-$Ni(OH)_2$, J. Am. Chem. Soc. 44 (2022) 15185–15192.
[51] P. Gandeepan, L.H. Finger, T.H. Meyer, L. Ackermann, 3d metallaelectrocatalysis for resource economical syntheses, Chem. Soc. Rev. 49 (2020) 4254–4272.
[52] X. Chen, S. Song, H. Li, G. Gözaydın, N. Yan, Expanding the boundary of biorefinery: organonitrogen chemicals from biomass, Acc. Chem. Res. 54 (2021) 1711–1722.
[53] M.T. Bender, Y.C. Lam, S. Hammes-Schiffer, K.-S. Choi, Unraveling two pathways for electrochemical alcohol and aldehyde oxidation on NiOOH, J. Am. Chem. Soc. 142 (2020) 21538–21547.
[54] R. Berenguer, A. La Rosa-Toro, C. Quijada, E. Morallón, Electrocatalytic oxidation of cyanide on copper-doped cobalt oxide electrodes, Appl. Catal. B 207 (2017) 286–296.
[55] Y. Huang, X. Chong, C. Liu, Y. Liang, B. Zhang, Boosting hydrogen production by anodic oxidation of primary amines over a NiSe nanorod electrode, Angew. Chem. Int. Ed. 57 (2018) 13163–13166.
[56] N. Sergienko, J. Radjenovic, Manganese oxide coated TiO_2 nanotube-based electrode for efficient and selective electrocatalytic sulfide oxidation to colloidal sulfur, Appl. Catal. B 296 (2021), 120383.
[57] R. Ge, Y. Wang, Z. Li, M. Xu, S.-M. Xu, H. Zhou, K. Ji, F. Chen, J. Zhou, H. Duan, Selective electrooxidation of biomass-derived alcohols to aldehydes in a neutral medium: promoted water dissociation over a nickel-oxide-supported ruthenium single-atom catalyst, Angew. Chem. Int. Ed. 61 (2022), e202200211.
[58] J. Li, L. Yao, D. Wu, J. King, S.S.C. Chuang, B. Liu, Z. Peng, Electrocatalytic methane oxidation to ethanol on iron-nickel hydroxide nanosheets, Appl. Catal. B 316 (2022), 121657.
[59] W. Chen, C. Xie, Y. Wang, Y. Zou, C.-L. Dong, Y.-C. Huang, Z. Xiao, Z. Wei, S. Du, C. Chen, B. Zhou, J. Ma, S. Wang, Activity origins and design principles of nickel-based catalysts for nucleophile electrooxidation, Chem 6 (2020) 2974–2993.
[60] W. Yang, X. Yang, J. Jia, C. Hou, H. Gao, Y. Mao, C. Wang, J. Lin, X. Luo, Oxygen vacancies confined in ultrathin nickel oxide nanosheets for enhanced electrocatalytic methanol oxidation, Appl. Catal. B 244 (2019) 1096–1102.